

## Conductivity Contrast and Tunneling Charge Transport in the Vortexlike Ferroelectric Domain Patterns of Multiferroic Hexagonal $\text{YMnO}_3$

E. Ruff,<sup>1</sup> S. Krohns,<sup>1</sup> M. Lilienblum,<sup>2</sup> D. Meier,<sup>2,3</sup> M. Fiebig,<sup>2</sup> P. Lunkenheimer,<sup>1,\*</sup> and A. Loidl<sup>1</sup>

<sup>1</sup>*Experimental Physics V, Center for Electronic Correlations and Magnetism, University of Augsburg, 86159 Augsburg, Germany*

<sup>2</sup>*Department of Materials, ETH Zurich, 8093 Zurich, Switzerland*

<sup>3</sup>*Department of Materials Science and Engineering, Norwegian University of Science and Technology, 7043 Trondheim, Norway*

(Received 11 July 2016; published 20 January 2017)

We deduce the intrinsic conductivity properties of the ferroelectric domain walls around the topologically protected domain vortex cores in multiferroic  $\text{YMnO}_3$ . This is achieved by performing a careful equivalent-circuit analysis of dielectric spectra measured in single-crystalline samples with different vortex densities. The conductivity contrast between the bulk domains and the less conducting domain boundaries is revealed to reach up to a factor of 500 at room temperature, depending on the sample preparation. Tunneling of localized defect charge carriers is the dominant charge-transport process in the domain walls that are depleted of mobile charge carriers. This work demonstrates that, via equivalent-circuit analysis, dielectric spectroscopy can provide valuable information on the intrinsic charge-transport properties of ferroelectric domain walls, which is of high relevance for the design of new domain-wall-based microelectronic devices.

DOI: 10.1103/PhysRevLett.118.036803

The hexagonal manganites  $\text{RMnO}_3$  ( $R = \text{Sc}, \text{Y}, \text{In},$  and  $\text{Dy-Lu}$ ) form a unique group of multiferroics where a geometrically driven mechanism triggers improper ferroelectricity [1]. Additional interest in this material class arose from the reported occurrence of vortexlike ferroelectric domain patterns [2–4]. Around the vortex cores, forming the centers of “cloverleaf” patterns of six domains, the polarization changes sign six times. These cores, evolving at a high-temperature structural transition [5], represent stable topological defects. Even strong electric fields lead only to a variation of ferroelectric domain sizes in these materials but are unable to completely eradicate unfavorable domains and to generate a monodomain state [2,6]. Moreover, there is a strict coupling of ferroelectric and antiferromagnetic domain walls (DWs), the latter forming at much lower temperatures around 100 K [7].

Recently, it was shown that these complex domain properties also may be of relevance from an application point of view: Conductive atomic-force microscopy (c-AFM) on  $\text{ErMnO}_3$  [4] and  $\text{HoMnO}_3$  [8] revealed that the conductance of the ferroelectric DWs is either enhanced or suppressed compared to the domains, being determined by the polarization orientation of the adjacent domains. As the DWs can be easily tuned by external fields, this opens the possibility of domain-boundary engineering and applications in microelectronics using the nanoscale DWs instead of the domains themselves as active device elements [9–13]. The hexagonal manganites seem especially suited for this kind of functionality: Their DWs are robust and represent persistent interfaces as they are attached to the vortex cores, but within these constraints they can be moved by an external field, thus enabling switching [4,12,13].

In general, insulating domain walls, also observed in various other systems as  $\text{SrMnO}_3$  thin films [14] and  $(\text{Ca}, \text{Sr})_3\text{Ti}_2\text{O}_7$  [15], have shifted into the focus of interest, due to their possible applications, e.g., as rewritable nanocapacitors. The conductivity contrast between these DWs and the domains should be as high as possible. However, there are literally no data available that unambiguously prove the intrinsic nature of the reduced conductance, and the mechanisms behind the residual domain-wall currents have not been tackled. For example, c-AFM, applied in Refs. [4,8] to hexagonal manganites, relies on the formation of Schottky-like barriers between the metallic tip and the semiconducting sample and thus essentially detects surface effects. Moreover, the current flow from the AFM tip to the bottom electrode leads to an ill-defined geometry. Thus, while the detected conductance variations of about one decade [4] or a factor of 4 [16] in  $\text{ErMnO}_3$  and of 25% in  $\text{HoMnO}_3$  [8] provide strong indications for different conductivities of domains and walls, no unequivocal information on the absolute value of the conductivity contrast is gathered. Recent photoemission electron-microscopy experiments on  $\text{ErMnO}_3$  have demonstrated the intrinsic nature of the conductivity variation between domains and DWs [17], but this technique also does not provide absolute values. These are fundamental problems that go beyond hexagonal manganites and also apply to functional ferroelectric domain walls in other systems.

Thus, new and unambiguous insight into the local transport behavior is highly desirable. Interestingly, bulk dielectric spectroscopy is able to reveal information about the electrical properties of different regions in heterogeneous samples, even without any efforts to sense the behavior of

specific sample regions by using microscopic contact geometries [18,19]. In the present work, we have employed dielectric spectroscopy to  $\text{YMnO}_3$ , probably the most studied hexagonal manganite, to determine the actual conductivity contrast between bulk (i.e., the domains) and domain boundaries with reduced conductance. There are several previous dielectric studies of this compound (e.g., [20–23]). Their results are inconsistent, which points to a strong influence of nonintrinsic effects and a considerable sample dependence of the dominant dielectric properties. We investigate two single crystals, measured as grown or subjected to different cooling rates after annealing above the structural phase transition ( $T_c \approx 1260$  K [5]), leading to distinct vortex densities [24,25].

Single crystals of  $\text{YMnO}_3$  were grown by the flux method (sample 1) and the floating-zone technique (sample 2) [5]. Their geometry is roughly platelike with the  $c$  axis vertical to the surface (sample 1: area  $4.7$  mm<sup>2</sup> and thickness  $0.3$  mm; sample 2:  $2.4$  mm<sup>2</sup> and  $0.4$  mm). Sample 1 was measured as grown and after annealing in  $\text{N}_2$  gas at  $1400$  K (well above  $T_c$  [5]), followed by cooling with  $1$  K/min down to  $900$  K to generate a defined vortex density (denoted as sample 1a) [24,25]. Sample 2 was annealed at  $1420$  K and cooled with  $10$  K/min. For the dielectric measurements, contacts of silver paint or sputtered platinum were applied to opposite faces of the crystals, ensuring an electrical field direction parallel to  $c$ . The dielectric constant  $\epsilon'$  and conductivity  $\sigma$  were determined using a frequency-response analyzer (Novocontrol Alpha-A Analyzer). Sample cooling and heating were achieved by a closed-cycle refrigerator and a homemade oven, with the sample in vacuum. For the determination of the vortex density, piezoresponse force microscopy (PFM) was performed at room temperature [4].

Figure 1 shows  $\epsilon'(T)$  and  $\sigma(T)$  of sample 1 at various frequencies between  $10$  and  $600$  K.  $\epsilon'(T)$  [Fig. 1(a)] exhibits a peak reaching “colossal” [18] values up to  $10^4$ . Its left flanks shift with frequency, signifying a relaxational process, and the overall behavior resembles that of so-called relaxor ferroelectrics [26,27]. However, one should be aware that the well-known nonintrinsic Maxwell-Wagner (MW) relaxations arising in heterogeneous samples in special cases can also mimic relaxor-ferroelectric behavior [18,28,29]. The low-temperature flanks of the  $\epsilon'(T)$  peaks seem to be composed of two consecutive steps indicating a large relaxorlike and an additional relaxation process with smaller amplitude, termed in the following relaxation 2 (at higher temperatures) and 1 (at lower temperatures), respectively. Relaxation steps are usually accompanied by peaks in the dielectric loss  $\epsilon''$ , which is proportional to  $\sigma'/\nu$ . In  $\sigma(T)$  [Fig. 1(b)], only the smaller relaxation 1 is revealed by a peak. It shows up only as a shoulder (e.g., at about  $200$  K for the  $1$  Hz curve) due to the superposition by the nonzero conductivity of the semiconducting sample, which strongly increases with temperature.

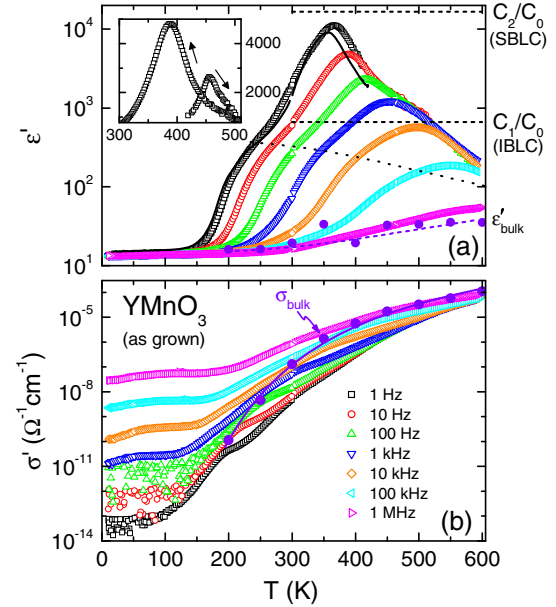


FIG. 1. Temperature dependence of (a)  $\epsilon'$  and (b)  $\sigma'$  of sample 1 with silver-paint contacts measured for various frequencies under cooling (open symbols). The solid line in (a) shows  $\epsilon'(T)$  at  $1$  Hz for the same sample, using sputtered platinum contacts. The dotted line in (a) roughly indicates the separation of relaxations 1 and 2 showing up at low and high temperatures, respectively. The two horizontal dashed lines in (a) indicate the capacitances (divided by the empty capacitance  $C_0$ ) of the two insulating regions used for the fits of the frequency-dependent data (Fig. 2). The closed circles in (a) represent  $\epsilon'_{\text{bulk}}$  as resulting from these fits; the corresponding dashed line is a guide for the eyes. The closed circles in (b) show the bulk dc conductivity as determined from the fits. The line in (b) is a fit of  $\sigma_{\text{bulk}}$  with the Arrhenius law [cf. Fig. 3(b)]. The inset in (a) shows  $\epsilon'(T)$  at  $1$  Hz, measured at the first heating run and the subsequent cooling run.

The larger relaxorlike mode 2 most likely is of MW type, arising from a so-called surface-barrier layer capacitor (SBLC) at the sample surface [18,30]. The missing  $\sigma'$  peak for this relaxation indicates similar conductance of the SBLC and the bulk [29]. Peaks in  $\epsilon'(T)$  have previously been observed in two other reports of the dielectric response of  $\text{YMnO}_3$  [21,22], however, at different temperatures and with different amplitudes, which speaks against an intrinsic origin. In addition, during our measurements at  $300$  K  $< T < 600$  K, involving several heating-cooling cycles, at the first heating run the peak occurred at a significantly higher temperature than at the subsequent runs [inset in Fig. 1(a)]. A change of the oxygen stoichiometry at the sample surface seems a reasonable explanation for this phenomenon, while it is unlikely that the stoichiometry of the whole sample changes at these relatively moderate temperatures [22]. Schottky diodes forming when metallic electrodes are applied to semiconducting samples are also often found to lead to MW relaxations [18,31,32]. To check for this possibility, we have performed measurements with different contact types [18]. They revealed only minor

deviations [cf. squares and solid line in Fig. 1(a)] indicating that Schottky-diode formation plays only a minor role in our sample. Adem *et al.* [23] recently reported a stronger influence of contact material on the giant relaxation mode found by them in  $\text{YMnO}_3$ , again pointing to the non-intrinsic and irreproducible nature of this surface-related spectral feature. In contrast to relaxation 2, we found the spectral features linked to relaxation 1 to be well reproducible in subsequent cooling and heating runs. We ascribe it to a MW relaxation caused by internal barrier layer capacitors (IBLCs) [33] arising from those parts of the ferroelectric DWs with low conductivity (the conducting parts of the DWs, also detected in Ref. [4], should not contribute to the dielectric properties).

Generally, thin layers within a sample, having lower conductivity than the bulk, act like capacitors (SBLCs or IBLCs) and lead to a MW relaxation and the typical signatures of relaxation processes: a step in  $\epsilon'(T, \nu)$  and a peak in  $\epsilon''(T, \nu)$ . Possible causes are Schottky diodes or nonstoichiometric surface layers (SBLCs) and grain boundaries or other IBLCs. The static limit of the dielectric constant,  $\epsilon_{s, \text{MW}}$ , observed at low frequencies [for  $\epsilon'(\nu)$  plots] or high temperatures [for  $\epsilon'(T)$ ], is artificially enhanced compared to the bulk dielectric constant  $\epsilon'_{\text{bulk}}$  by a factor given by the ratio of the sample thickness  $d$  and overall layer thickness  $D_l$ , i.e.,  $\epsilon_{s, \text{MW}} \propto d/D_l$  [18] (note that  $D_l$  is the summed-up, effective DW thickness and not the real thickness of a single DW). This is strictly valid if making the reasonable assumption that the intrinsic  $\epsilon'$  of the charge-carrier-depleted layers is of the same order as for the bulk. As  $d/D_l$  can become very large, this explains the apparently

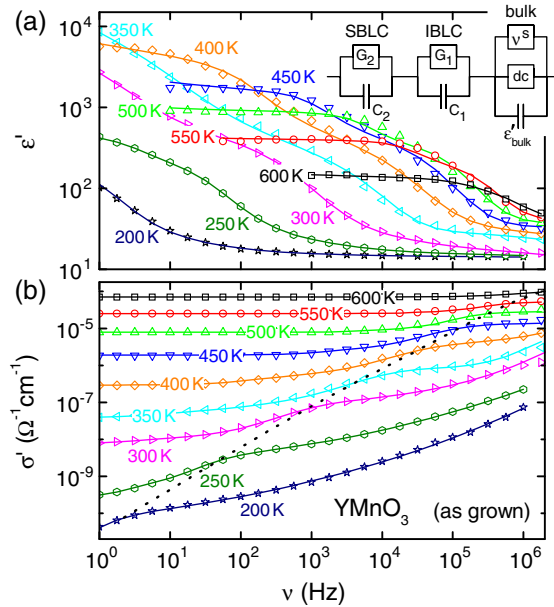


FIG. 2. (a)  $\epsilon''$  and (b)  $\sigma'$  spectra of sample 1. The solid lines in (a) and (b) are fits using the equivalent circuit indicated in (a) (see the text), simultaneously performed for  $\epsilon'(\nu)$  and  $\sigma'(\nu)$ . The dotted line in (b) connects the shoulders arising from relaxation 1.

colossal values of  $\epsilon'$  arising from surface effects in some materials [18,31–33] and in the present case of relaxation 2.

To obtain quantitative information, we have analyzed the frequency dependence of the measured dielectric properties as shown for sample 1 in Fig. 2. Here in  $\epsilon'(\nu)$  [Fig. 2(a)] two successive steps are observed corresponding to relaxations 2 (at low frequencies) and 1 (high frequencies). The shoulders revealed in  $\sigma'(\nu)$  [connected by the dotted line in Fig. 2(b)] arise from relaxation 1. At low temperatures and high frequencies, the bulk properties dominate the data (e.g., for 300 K above about 3 kHz) as the insulating thin layers, acting like lossy capacitors, become shortened [18,31]. For the bulk dielectric constant,  $\epsilon'_{\text{bulk}} \approx 20$  is found. The bulk conductivity shows a nearly frequency-independent region signifying dc conductivity  $\sigma_{\text{dc}}$ , followed by a power-law increase indicating hopping conductivity [18,34].

The lines in Fig. 2 are fits using the equivalent circuit shown in Fig. 2(a). The SBLCs and IBLCs, schematically indicated in Fig. 3(a), are both modeled by parallel  $RC$  circuits ( $C_2 || G_2$  and  $C_1 || G_1$ , respectively, with  $G$  the conductances) [18,31,33]. For the bulk part of the sample, a capacitor accounting for the intrinsic  $\epsilon'_{\text{bulk}}$ , a resistor for  $\sigma_{\text{dc}}$ , and an element with a frequency-dependent conductivity  $\sigma' \propto \sigma'' \propto \nu^s$  with  $s < 1$  is used [18,31]. The latter corresponds to Jonscher's universal dielectric response [35] covering the mentioned increase of  $\sigma'(\nu)$  due to hopping transport. Notably, perfect fits of the complete data set are possible with temperature-independent capacitors  $C_1$

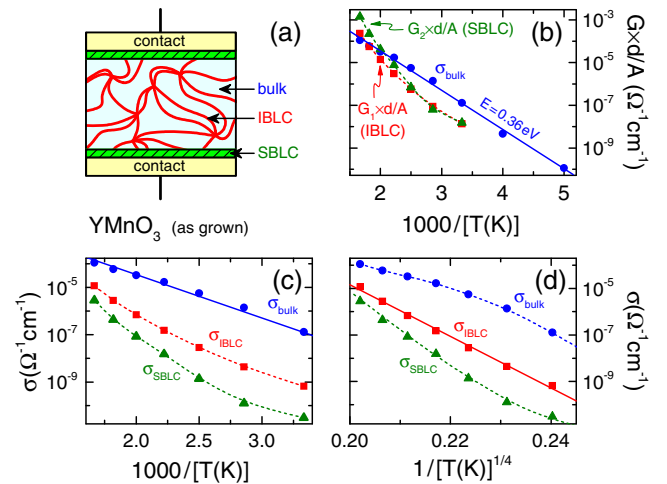


FIG. 3. (a) Schematic sample cross section (not to scale) indicating bulk, SBLC, and IBLC regions, where the IBLCs arise from the DWs (this picture is somewhat oversimplified, as only part of the DWs have low conductivity [4]). (b) Arrhenius representation of the bulk dc conductivity and apparent layer conductivities (conductances multiplied by the bulk geometry factor  $d/A$ ) of sample 1 as obtained from the fits shown in Fig. 2. (c) Bulk dc conductivity and true layer conductivities calculated as described in the text. (d) The same as (c) but using a representation that linearizes  $\sigma(T)$  for variable range hopping. The solid lines in (b)–(d) are linear fits; the dashed lines are guides to the eye.

and  $C_2$  [horizontal dashed lines in Fig. 1(a)] as usually found for SBLCs and IBLCs [18,31–33].  $\epsilon'_{\text{bulk}}(T)$  as resulting from the fits is included in Fig. 1(a) (closed circles). It varies between about 15 and 35. Obviously, this equivalent-circuit approach provides a good description of our data without assuming contributions from segmental DW oscillations found in some canonical ferroelectrics [36].

In the following, we deduce the intrinsic conductivities of the DWs and SBLCs from the fit results. Figure 3(b) shows the apparent conductivities obtained from the fits, which correspond to the conductances of the equivalent circuit multiplied by the bulk geometry factor  $d/A$  ( $A$ , sample area). However, only for the bulk, this represents the *intrinsic* conductivity  $\sigma_{\text{bulk}}$ . The latter is also included in Fig. 1(b) revealing the typical behavior for MW relaxations [18,37,38].  $\sigma_{\text{bulk}}$  follows the Arrhenius law with an activation energy of 0.36 eV. The same value was also found at the highest frequencies and lowest temperatures investigated in Ref. [21], where obviously the intrinsic bulk response was detected. Figure 3(b) reveals that the layer conductances cross the bulk curve at high temperatures. Such a behavior can cause an apparent relaxor-ferroelectric signature in  $\epsilon'(T, \nu)$  as indeed observed in Fig. 1 [18,29].

In contrast to the bulk, for the layers the quantity  $G \times d/A$  plotted in Fig. 3(b) represents only the *apparent* conductivity, because their overall thickness  $D_l$  is smaller than the sample thickness  $d$ . To calculate the *intrinsic* layer conductivities  $\sigma_{\text{SBLC}}$  and  $\sigma_{\text{IBLC}}$ ,  $G \times d/A$  shown in Fig. 3(b) has to be divided by  $d/D_l$ . This ratio can be estimated from our fit results if considering the mentioned enhancement of  $\epsilon_{s,\text{MW}}$  of the corresponding MW relaxation, which is determined by the ratio of the sample and overall layer thickness, i.e.,  $\epsilon_{s,\text{MW}}/\epsilon'_{\text{bulk}} = d/D_l$ . This relation is valid if making the reasonable assumption of homogeneity of  $\epsilon'$  all over the sample. Using an average value of  $\epsilon'_{\text{bulk}} \approx 20$  and the  $\epsilon_{s,\text{MW}}$  values obtained from the fits, this ratio is about 33 for the IBLCs and 830 for the SBLCs. The intrinsic layer conductivities calculated using these values are shown in Fig. 3(c), together with  $\sigma_{\text{bulk}}$ .  $\sigma_{\text{SBLC}}$  is by about 2–4 decades lower than  $\sigma_{\text{bulk}}$ . Of special interest is the result for  $\sigma_{\text{IBLC}}$  revealing that, at room temperature, the conductivity of the insulating DWs is by more than two decades lower than for the bulk ( $\sigma_{\text{bulk}}/\sigma_{\text{IBLC}} \approx 190$ ). Thus, the conductivity contrast is significantly stronger than the conductance ratios obtained for two related hexagonal manganites from c-AFM measurements [4,8], which do not reveal absolute values of the conductivities. It should be noted that the obtained DW conductivity is a representative value of the insulating parts of the DWs and our results do not exclude conductivity variations in dependence of polarization orientation as detected in Refs. [4,8].

Figure 3(c) demonstrates clear deviations of  $\sigma_{\text{IBLC}}(T)$  from thermally activated behavior. Instead, it follows  $\sigma_{\text{IBLC}} \sim \exp[-(T_0/T)^{1/4}]$ , as predicted for variable range hopping [Fig. 3(d)] pointing to phonon-assisted tunneling of Anderson-localized electrons or holes [39]. In Ref. [16],

for  $\text{ErMnO}_3$  it was explicitly demonstrated that the insulating DWs are depleted from mobile charge carriers (holes). From our results, we conclude that the charge transport in these DWs is dominated by tunneling of the remaining localized charge carriers. Interestingly, recent electron-energy loss spectroscopy and density-functional theory calculations suggest charge transport via minority charge carriers (electrons) for the insulating DWs at a sufficiently large voltage [40]. Their localized nature and small carrier density of about 0.1 per Mn ion is well consistent with the occurrence of hopping charge transport as found in the present work.

As shown before [24,25], annealing hexagonal manganites above  $T_c$  and subsequent cooling with different rates leads to well-defined vortex densities which depend on the cooling rate. The right part of Fig. 4 presents PFM images of the annealed samples 1a and 2, exhibiting the typical domain patterns [2,4,24]. A vortex density  $\rho_v$  of about  $4 \times 10^4/\text{mm}^2$  is deduced for sample 1a, while sample 2 has a significantly higher  $\rho_v$  of about  $1.5 \times 10^6/\text{mm}^2$ . The dielectric properties of these samples also reveal the presence of two relaxation processes, which were interpreted and analyzed in the same way as for sample 1 [29]. The obtained intrinsic conductivities are shown in Fig. 4. For the annealed sample 1a, the bulk conductivity at room temperature is by more than two decades higher than for the as-grown state of this sample, and a lower energy barrier of 0.26 eV is found. Most interestingly, we obtain a conductivity contrast between the bulk and insulating DWs of about 500 at room temperature, even higher than in the untempered sample. In marked contrast, while sample 2 exhibits a bulk conductivity and energy barrier of similar order as for the untempered sample 1, it seems to have a much smaller conductivity contrast of about 1.3 only at

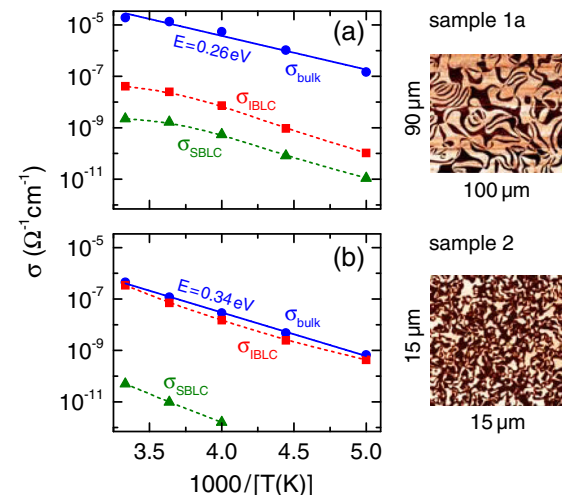


FIG. 4. Bulk dc conductivity and true layer conductivities of the annealed samples 1a (a) and 2 (b), deduced from the equivalent-circuit analysis as described in the text. The solid lines in both frames are linear fits; the dashed lines are guides to the eye. At the right side of the figures, PFM images of the  $ab$  sample surfaces are shown.

room temperature. Different annealing-cooling cycles obviously have a pronounced effect on the MW relaxations in  $\text{YMnO}_3$  [29] pointing to marked variations of bulk and DW conductivity. Moreover, the different crystal-growth procedure of sample 2 may also play a role for its different behavior. Further work is necessary to systematically investigate the dependence of the intrinsic conductivities in the hexagonal manganites on the sample history.

In summary, we have measured the dielectric properties of single-crystalline  $\text{YMnO}_3$  and performed a detailed equivalent-circuit analysis of the obtained spectra. From this, we were able to determine absolute values of the conductivity of the ferroelectric DWs with suppressed conductance and of the conductivity contrast between the domains and DWs. For the latter, we find values up to 500 at room temperature and indications for a strong dependence on the thermal history and crystal-growth procedure of the samples. The charge transport in the insulating DWs is dominated by the tunneling of localized charge carriers. These results demonstrate that dielectric spectroscopy can disclose the intrinsic conductivity properties of ferroelectric DWs, which is a prerequisite for the development of new domain-wall-based nanotechnology.

We thank N. A. Spaldin for stimulating discussions. This work was supported by the Deutsche Forschungsgemeinschaft through the Transregional Collaborative Research Center TRR 80 (Augsburg, Munich, Stuttgart), by the BMBF via ENREKON 03EK3015, and by SNSF Grant No. 200021\_149192/1.

\*Corresponding author.

Peter.Lunkenheimer@Physik.Uni-Augsburg.de

- [1] B. B. Van Aken, T. T. M. Palstra, A. Filippetti, and N. A. Spaldin, *Nat. Mater.* **3**, 164 (2004).
- [2] T. Choi, Y. Horibe, H. T. Yi, Y. J. Choi, W. Wu, and S.-W. Cheong, *Nat. Mater.* **9**, 253 (2010).
- [3] M. Mostovoy, *Nat. Mater.* **9**, 188 (2010).
- [4] D. Meier, J. Seidel, A. Cano, K. Delaney, Y. Kumagai, M. Mostovoy, N. A. Spaldin, R. Ramesh, and M. Fiebig, *Nat. Mater.* **11**, 284 (2012).
- [5] M. Lilienblum, T. Lottermoser, S. Manz, S. M. Selbach, A. Cano, and M. Fiebig, *Nat. Phys.* **11**, 1070 (2015).
- [6] T. Jungk, Á. Hoffmann, M. Fiebig, and E. Soergel, *Appl. Phys. Lett.* **97**, 012904 (2010).
- [7] M. Fiebig, Th. Lottermoser, D. Fröhlich, A. V. Goltsev, and R. V. Pisarev, *Nature (London)* **419**, 818 (2002).
- [8] W. Wu, Y. Horibe, N. Lee, S.-W. Cheong, and J. R. Guest, *Phys. Rev. Lett.* **108**, 077203 (2012).
- [9] E. Salje and H. Zhang, *Phase Transitions* **82**, 452 (2009).
- [10] H. Béa and P. Paruch, *Nat. Mater.* **8**, 168 (2009).
- [11] G. Catalan, J. Seidel, R. Ramesh, and J. F. Scott, *Rev. Mod. Phys.* **84**, 119 (2012).
- [12] M. Fiebig, *Phil. Trans. R. Soc. A* **370**, 4972 (2012).
- [13] D. Meier, *J. Phys. Condens. Matter* **27**, 463003 (2015).
- [14] C. Becher, L. Maurel, U. Aschauer, M. Lilienblum, C. Magén, D. Meier, E. Langenberg, M. Trassin, J. Blasco, I. P. Krug, P. A. Algarabel, N. A. Spaldin, J. A. Pardo, and M. Fiebig, *Nat. Nanotechnol.* **10**, 661 (2015).
- [15] Y. S. Oh, X. Luo, F.-T. Huang, Y. Wang, and S.-W. Cheong, *Nat. Mater.* **14**, 407 (2015).
- [16] J. Schaab, A. Cano, M. Lilienblum, Z. Yan, E. Bourret, R. Ramesh, M. Fiebig, and D. Meier, *Adv. Electron. Mater.* **2**, 1500195 (2016).
- [17] J. Schaab, I. P. Krug, F. Nickel, D. M. Gottlob, H. Doğanay, A. Cano, M. Hentschel, Z. Yan, E. Bourret, C. M. Schneider, R. Ramesh, and D. Meier, *Appl. Phys. Lett.* **104**, 232904 (2014).
- [18] P. Lunkenheimer, S. Krohns, S. Riegg, S. G. Ebbinghaus, A. Reller, and A. Loidl, *Eur. Phys. J. Spec. Top.* **180**, 61 (2010).
- [19] V. Bobnar, P. Lunkenheimer, M. Paraskevopoulos, and A. Loidl, *Phys. Rev. B* **65**, 184403 (2002).
- [20] I. G. Ismailzade and S. A. Kizhaev, *Sov. Phys. Solid State* **7**, 236 (1965).
- [21] M. Tomczyk, P. M. Vilarinho, A. Moreira, and A. Almeida, *J. Appl. Phys.* **110**, 064116 (2011).
- [22] P. Ren, H. Fan, and X. Wang, *Appl. Phys. Lett.* **103**, 152905 (2013).
- [23] U. Adem, N. Mufti, A. A. Nugroho, G. Catalan, B. Noheda, and T. T. M. Palstra, *J. Alloys Compd.* **638**, 228 (2015).
- [24] S. C. Chae, N. Lee, Y. Horibe, M. Tanimura, S. Mori, B. Gao, S. Carr, and S.-W. Cheong, *Phys. Rev. Lett.* **108**, 167603 (2012).
- [25] S. M. Griffin, M. Lilienblum, K. T. Delaney, Y. Kumagai, M. Fiebig, and N. A. Spaldin, *Phys. Rev. X* **2**, 041022 (2012).
- [26] L. E. Cross, *Ferroelectrics* **76**, 241 (1987).
- [27] A. Levstik, Z. Kutnjak, C. Filipič, and R. Pirc, *Phys. Rev. B* **57**, 11204 (1998).
- [28] G. Catalan, D. O'Neill, R. M. Bowman, and J. M. Gregg, *Appl. Phys. Lett.* **77**, 3078 (2000).
- [29] See Supplemental Material at <http://link.aps.org/supplemental/10.1103/PhysRevLett.118.036803> for more details on the nonintrinsic relaxor behavior and the dielectric results for samples 1a and 2.
- [30] S. Krohns, P. Lunkenheimer, S. G. Ebbinghaus, and A. Loidl, *Appl. Phys. Lett.* **91**, 022910 (2007).
- [31] P. Lunkenheimer, V. Bobnar, A. V. Pronin, A. I. Ritus, A. A. Volkov, and A. Loidl, *Phys. Rev. B* **66**, 052105 (2002).
- [32] P. Lunkenheimer, R. Fichtl, S. G. Ebbinghaus, and A. Loidl, *Phys. Rev. B* **70**, 172102 (2004).
- [33] D. C. Sinclair, T. B. Adams, F. D. Morrison, and A. R. West, *Appl. Phys. Lett.* **80**, 2153 (2002).
- [34] S. R. Elliott, *Adv. Phys.* **36**, 135 (1987).
- [35] A. K. Jonscher, *Nature (London)* **267**, 673 (1977).
- [36] W. Kleemann, *Annu. Rev. Mater. Res.* **37**, 415 (2007).
- [37] A. Seeger, P. Lunkenheimer, J. Hemberger, A. A. Mukhin, V. Yu. Ivanov, A. M. Balbashov, and A. Loidl, *J. Phys. Condens. Matter* **11**, 3273 (1999).
- [38] A. Ruff, S. Krohns, F. Schrettle, V. Tsurkan, P. Lunkenheimer, and A. Loidl, *Eur. Phys. J. B* **85**, 290 (2012).
- [39] N. F. Mott and E. A. Davis, *Electronic Processes in Non-Crystalline Materials* (Clarendon Press, Oxford, 1979).
- [40] J. A. Mundy, J. Schaab, Y. Kumagai, A. Cano, M. Stengel, I. P. Krug, D. M. Gottlob, H. Doganay, M. E. Holtz, R. Held, Z. Yan, E. Bourret, C. M. Schneider, D. G. Schlom, D. A. Muller, R. Ramesh, N. A. Spaldin, and D. Meier (unpublished).